Electronic Supplementary Material (ESI) for Journal of Materials Chemistry A.

Electronic Supplementary Information (ESI)

Ultrafast Cathode Characteristics of a Nano-$V_2(PO_4)_3$ Carbon Composite for Rechargeable Magnesium Batteries

Yuta Harada[a] , Yu Chikaoka *[ab], Marina Kasai[a], Kyoya Koizumi[a] , Etsuro Iwama [ab], Naohisa Okita[a], Yuki Orikasa[c], Wako Naoi[d], and Katsuhiko Naoi *[abe]

[a] Department of Applied Chemistry, Tokyo University of Agriculture & Technology, 2-24-16 Naka-cho, Koganei, Tokyo 184-8558, Japan

[b] Global Innovation Research Organization, Tokyo University of Agriculture & Technology, 2-24-16 Naka-cho, Koganei, Tokyo, 184-8588 Japan

[c] Department of Applied Chemistry, Ritsumeikan University, 1-1-1 Nojihigashi, Kusatsu 525-8577, Japan

[d] Division of Art and Innovative Technologies, K & W Inc., 1-3-16-901 Higashi, Kunitachi, Tokyo 186-0002, Japan

[e] Advanced Capacitor Research Center, Tokyo University of Agriculture & Technology, 2-24-16 Naka-cho, Koganei, Tokyo 184-8558, Japan

* Corresponding Authors: chika@go.tuat.ac.jp / k-naoi@cc.tuat.ac.jp

Detailed charge–discharge profiles of VP/KB(5:5) cathode in three-electrode cells

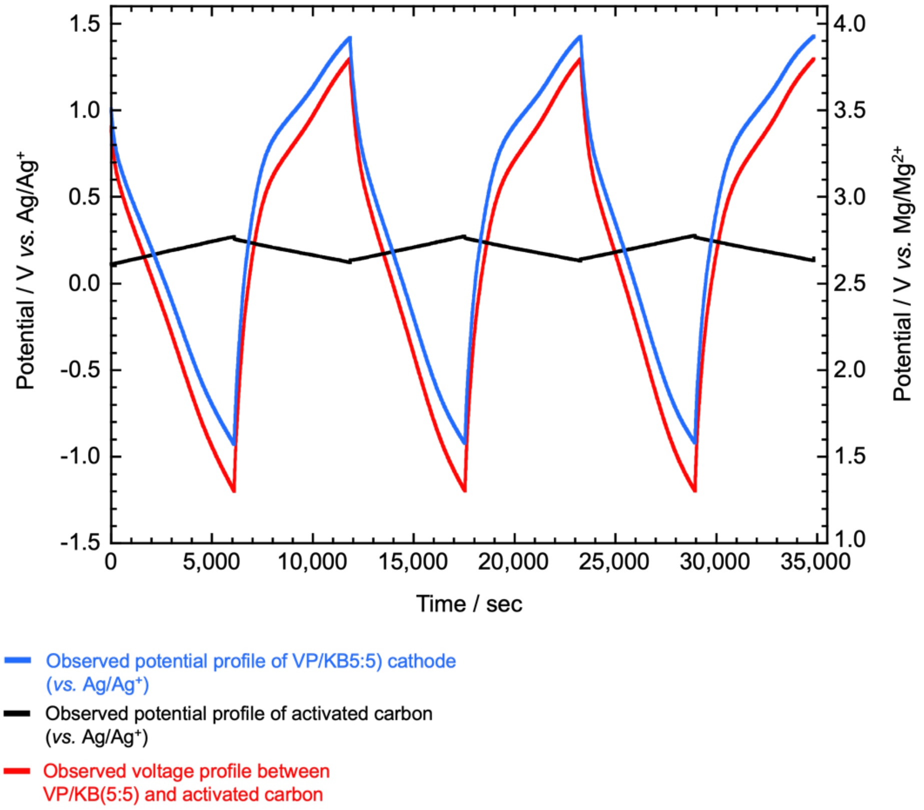

Figure S1. Charge–discharge profiles of VP/KB(5:5) with [0.5 M Mg(TFSA)$_2$ + 1 M SBPBF$_4$/DMC] in three-electrode cells equipped with the Ag/Ag$^+$ reference electrode at 1C-rate (1C-rate = 131.5 mAh g^{-1} of $V_2(PO_4)_3$ active material) for the first three cycles. During the charge–discharge tests of VP/KB(5:5) conducted versus the activated carbon (AC) electrode in the voltage range of 1.3 to −1.2 V *vs*. AC, the reference potential of the AC electrode was almost constant (around 0.2 V *vs.* Ag/Ag$^+$), whereas that of $V_2(PO_4)_3$ varied from approximately 1.4 to −0.9 V *vs.* Ag/Ag$^+$. Thus, the potential of the $V_2(PO_4)_3$ electrode was determined to be 1.4 to −0.9 V *vs.* Ag/Ag$^+$ (equivalent to 1.1–3.6 V *vs.* Mg/Mg^{2+}).

X-ray diffraction (XRD) patterns of KB and MWCNTs

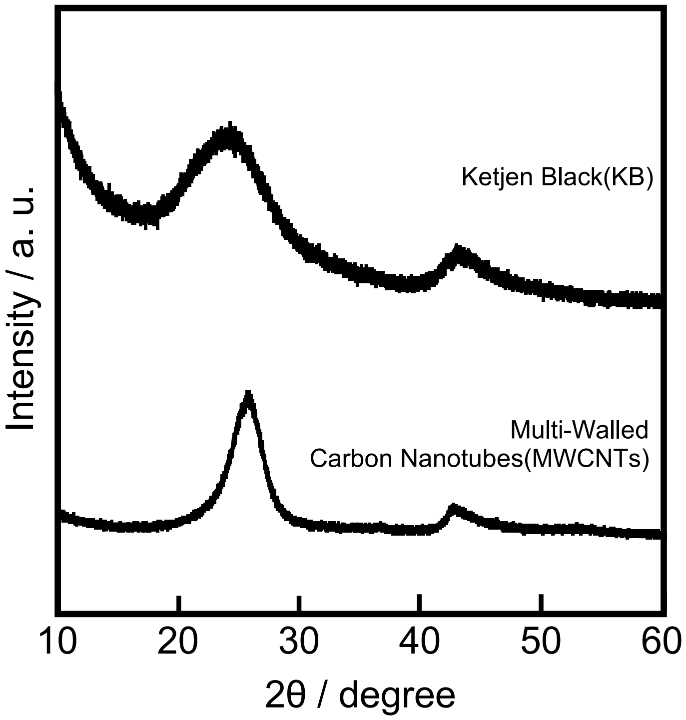

Figure S2. XRD patterns of Ketjenblack (KB) and Multiwalled carbon nanotubes (MWCNTs).

Lattice parameters and crystallite size of LVP/carbon composites[1]

Table S1. The lattice parameters (*a*, *b*, *c*, and *V*) and crystallite sizes of the LVP/KB and LVP/MWCNT composites. Lattice parameters were calculated by Rietveld refinement. The full widths at half-maximums (FWHMs) obtained by the LVP (020) peak have been converted to the apparent average crystallite size based on the Scherrer equation. Scherrer equation for the calculation of particle size is $D = K\lambda/\beta\cos\theta$ where *K* is the Scherrer constant, λ is the wavelength of the X-ray beam used (1.54184 Å), β is the FWHM of the peak, and θ is the Bragg angle.

	Space group	a / Å	b / Å	c / Å	β / °	V / Å^3	R_{wp}	Crystallite sizes/ Å
LVP/KB(7:3)	$P2_1/n$	8.596(2)	8.586(2)	12.046(3)	90.418(9)	889.0(4)	9.68	391(30)
LVP/KB(6:4)	$P2_1/n$	8.600(2)	8.5880(19)	12.049(3)	90.443(10)	889.9(4)	7.68	392(16)
LVP/KB(5:5)	$P2_1/n$	8.603(3)	8.596(3)	12.062(5)	90.413(15)	892.0(6)	7.03	285(18)
LVP/KB(4:6)	$P2_1/n$	8.624(5)	8.604(4)	12.072(7)	90.541(15)	895.7(8)	4.51	297(26)
LVP/MWCNT(5:5)	$P2_1/n$	8.6113(10)	8.6057(10)	12.0574(15)	90.439(6)	893.50(19)	7.82	368(7)
$Li_3V_2(PO_4)_3$ [1]	$P2_1/n$	8.606	8.591	12.036	90.61	899.8	-	-

Charge–discharge profiles of LVP/KB and LVP/MWNCT for Li electrolyte

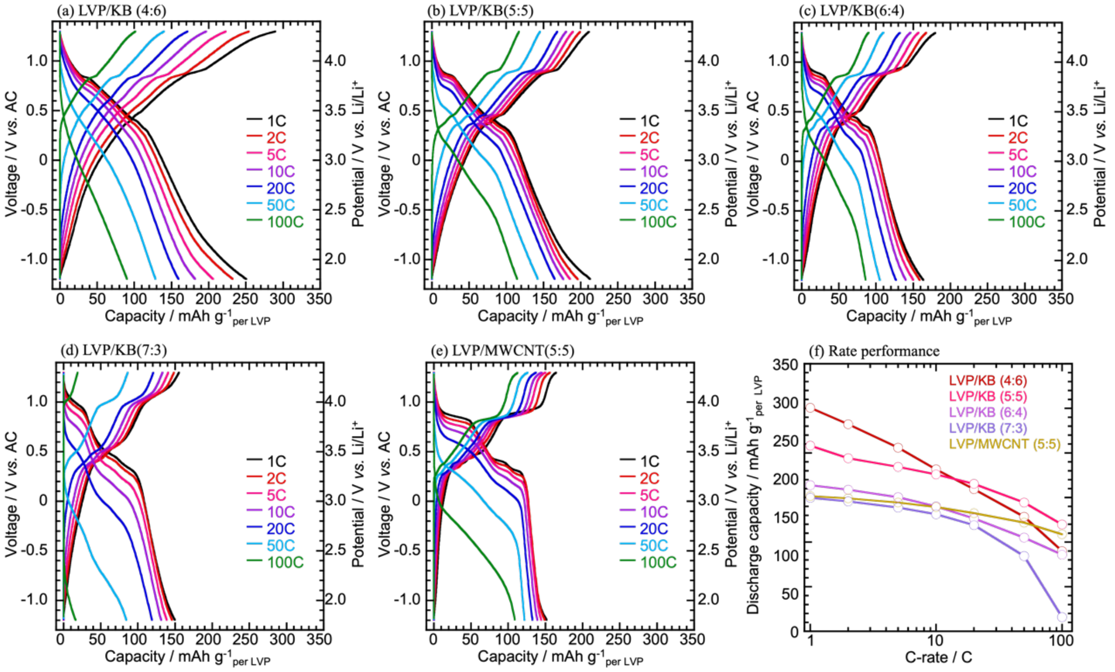

Figure S3. Charge–discharge plots of **(a)** LVP/KB(4:6), **(b)** LVP/KB(5:5), **(c)** LVP/KB(6:4), **(d)** LVP/KB(7:3), and **(e)** LVP/MWCNT(5:5) at 1–100C-rates (1C-rate = 131.5 mAh g^{-1} of $Li_3V_2(PO_4)_3$ active material). **(f)** Capacity–C-rate plots of LVP/carbon composites. **[Cell Conditions for half-cell evaluation]:** Working electrode(PE): LVP/Carbon composites : PVDF = 9:1, counter electrode(NE): AC : KB : PTFE = 80 : 10 : 10, electrolyte : 1.0 M $LiPF_6$ / EC:DEC (1:1 vol.), voltage range : -1.2-1.3 V *vs*. AC, temperature : 25 °C.

Net exhibited capacities of KB and LVP using Li^+-based electrolyte

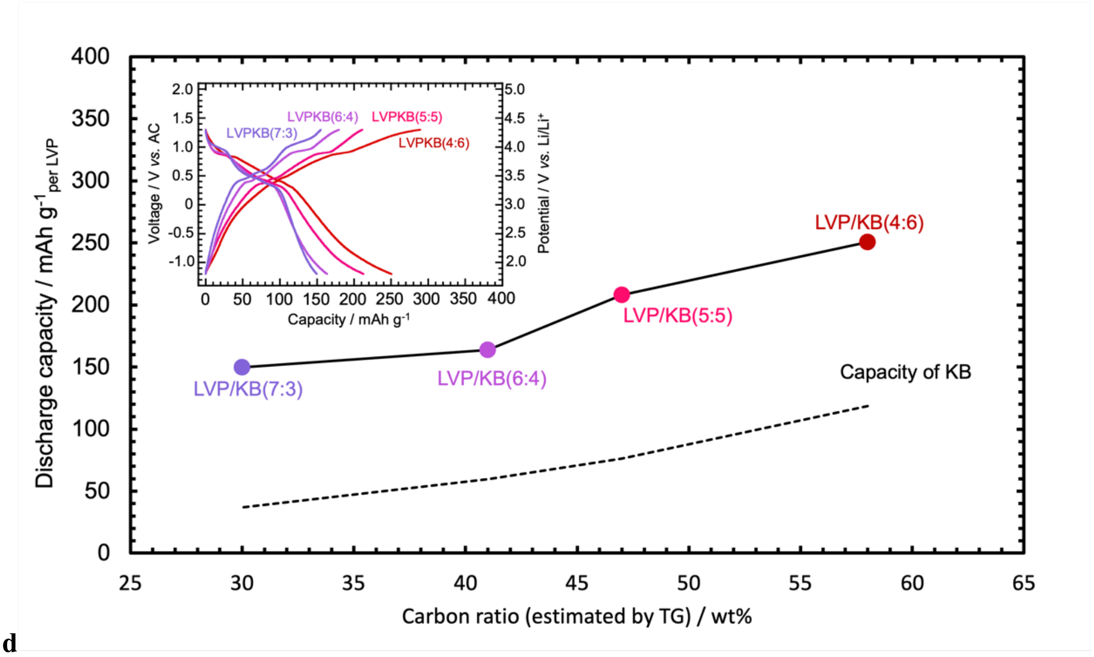

Figure S4. Exhibited capacities of LVP/KB with various carbon contents using Li^+-based electrolytes at 1C-rate and the KB-derived capacity calculated from Fig. S5 (dash line). The value of the carbon content of VP/KB was obtained from TGA. Inset: charge–discharge plots of each LVP/KB composite at 1C-rate. The net LVP capacities (LVP/KB capacity minus KB-derived capacity) were 113.5 mAh g^{-1} for LVP/KB(4:6), 117.7 mAh g^{-1} for LVP/KB(5:5), 94.1 mAh g^{-1} for LVP/KB(6:4) and 106.3 mAh g^{-1} for LVP/KB(7:3), respectively.

Charge-discharge characteristics of KB using Mg^{2+}-based electrolyte

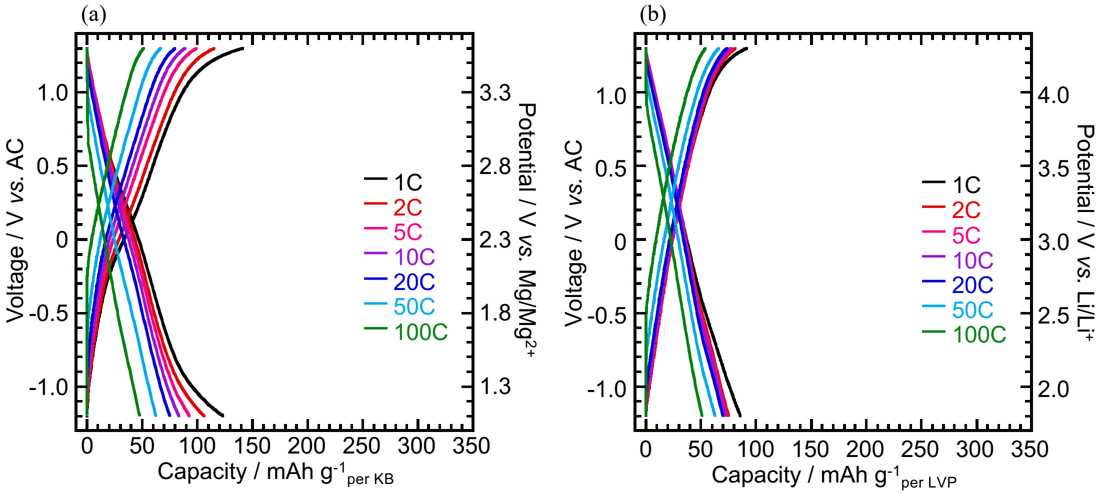

Figure S5. Charge–discharge plots of KB in **(a)** 0.5 M $Mg(TFSA)_2$ + 1 M $SBPBF_4$/DMC and **(b)** 1.0 M $LiPF_6$ / EC:DEC (1:1 vol.) at a rate of 1–100C-rate (1C-rate = 131.5 mAh g^{-1} of KB). **[Cell Conditions for full-cell evaluation]:**Working electrode**(**PE): KB : PVDF = 9:1, counter electrode: AC : KB : PTFE = 80 : 10 : 10, electrolyte : 0.5 M $Mg(TFSA)_2$ + 1 M $SBPBF_4$/DMC or 1.0 M $LiPF_6$ / EC:DEC (1:1 vol.), voltage range : -1.2-1.3 V *vs*. AC, temperature : 25 °C

STEM images and electron energy-loss spectroscopy (EELS) results of VP/KB(5:5)

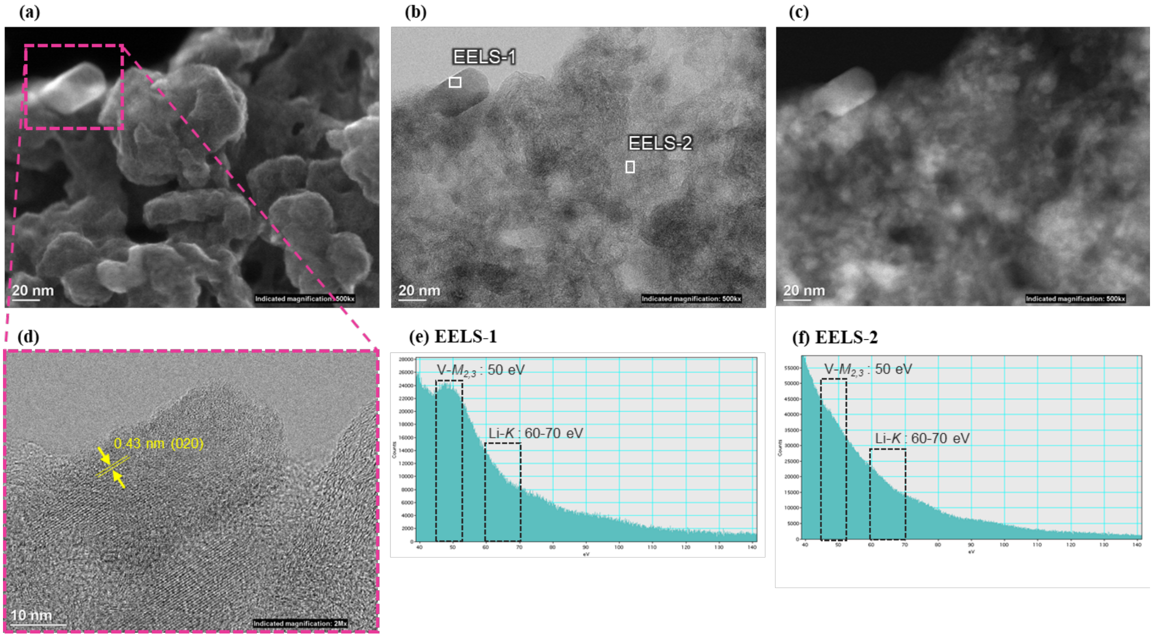

Figure S6. **(a)** Scanning transmission electron microscopy (STEM) image **(b)** bright-field STEM image **(c)** dark-field STEM image **(d)** high-resolution TEM images of delithiated VP/KB(5:5). Clear lattice fringes of *d* = 0.43 nm appear, corresponding to the (020) planes of monoclinic $Li_3V_2(PO_4)_3$ **(e-f)** EELS of VP/KB(5:5). EELS was used to examine the areas within the two white rectangles (labeled EELS-1 and EELS-2) in Fig. S6b, respectively. In EELS-1 (Fig. S6e), the V M-edge was observed, indicating the presence of VP particles. In contrast, in EELS-2 (Fig. S6f), the V M-edge was not observed, indicating the presence of only KB.

STEM and Energy Dispersive X-ray Spectroscopy (EDX) results of Mg^{2+} inserted VP/KB(5:5)

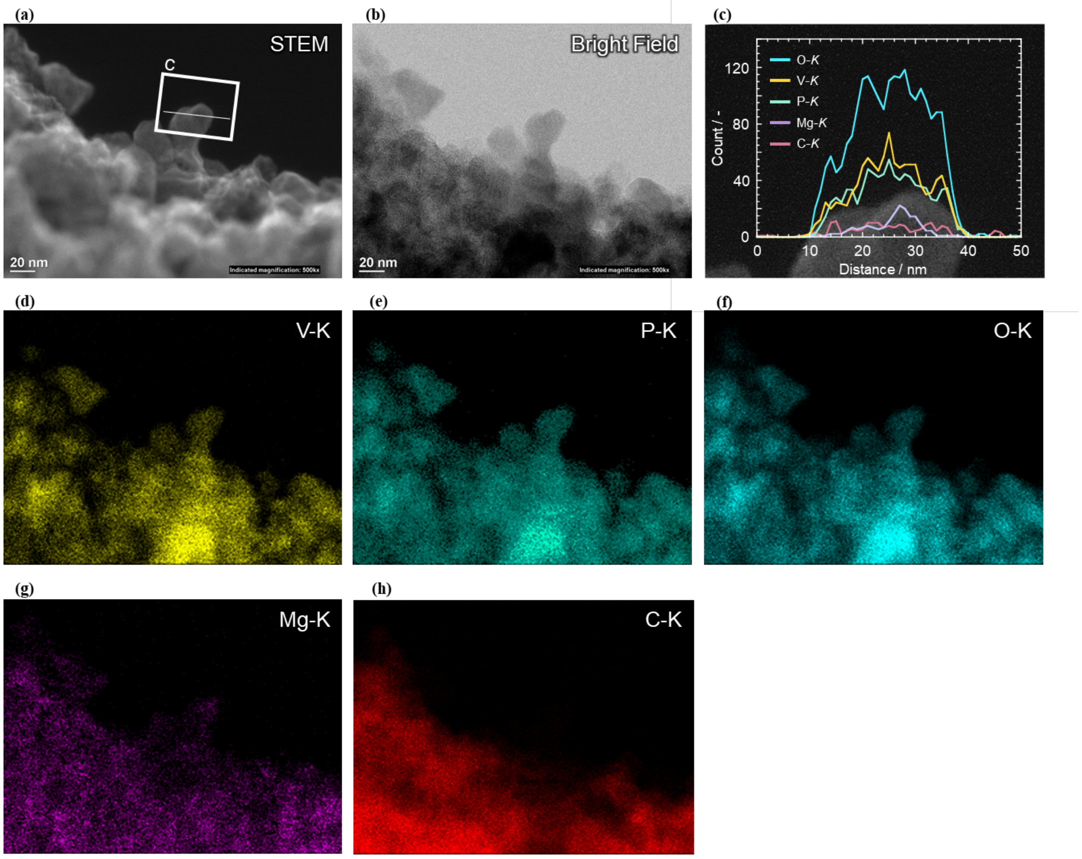

Figure S7. **(a)** STEM image of VP/KB(5:5) after Mg^{2+}-insertion (1.1 V *vs.* Mg/Mg^{2+}), **(b)** bright-field STEM image, **(c)** STEM images with EDX line scan mapping of the areas demarcated by white rectangles in Fig. S7a. In this area, the O-K, V-K, and P-K edges were observed, indicating the presence of VP particles. Mg-K edges were also observed, suggesting the insertion of Mg^{2+} into the VP particles. **(d-h)** EDX elemental mapping of VP/KB(5:5) with inserted Mg^{2+}. Mg-K edges were observed in the areas where the V-K, P-K, and O-K edges were observed. Mg^{2+} was inserted into VP/KB (5:5) by charging at 1C-rate to 1.3 V *vs*. AC (corresponding to 3.6 V *vs*. Mg/Mg^{2+}) then discharging to −1.2 V *vs*. AC (corresponding to 1.1 V *vs*. Mg/Mg^{2+}).

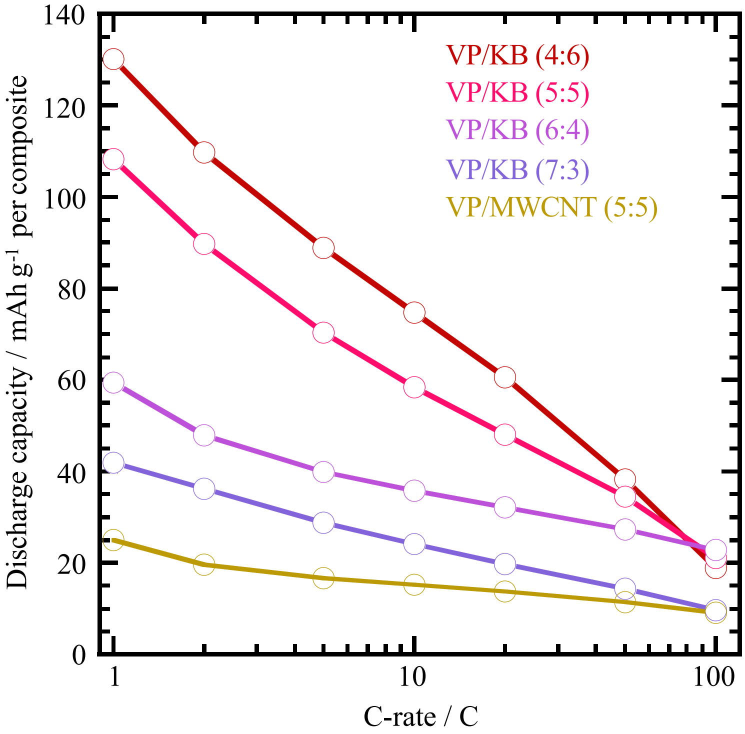

Figure S8. Capacity *vs.* C-rate plots of LVP/KB and LVP/MWCNT composites. Discharge capacity was calculated per weight of composite.

Net exhibited capacity of VP/KB and KB using Mg^{2+}-based electrolyte

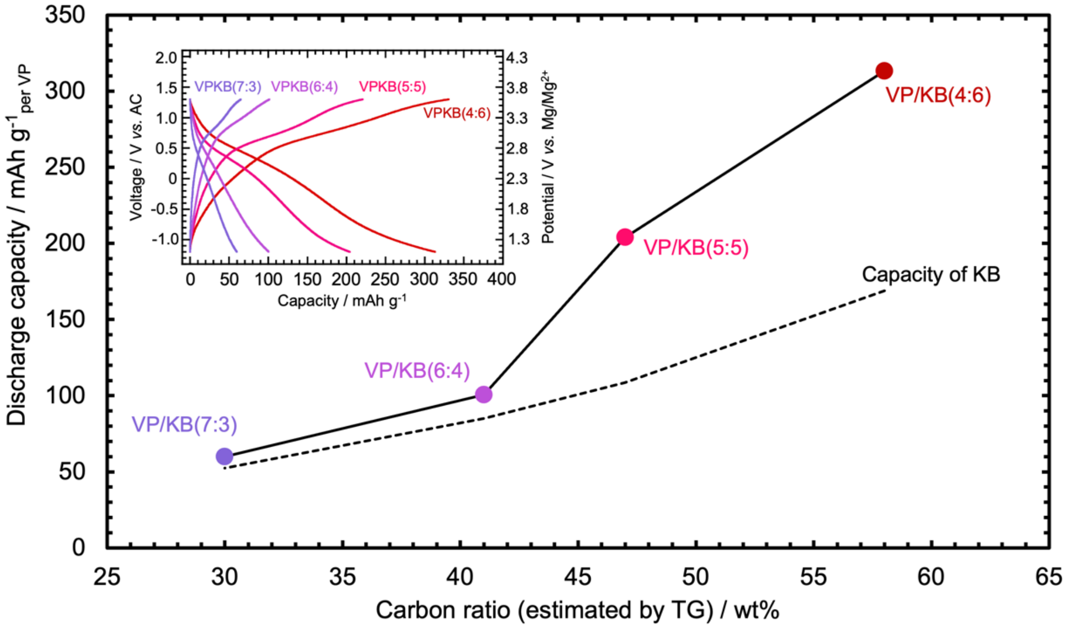

Figure S9. Exhibited capacities of VP/KB with various carbon contents using Mg^{2+} electrolytes at 1C-rate and the KB-derived capacity calculated from Fig. S5 (dashed line). The value of the carbon content of VP/KB was obtained from TGA. Inset: charge–discharge plots of each VP/KB composite at 1C-rate. The net VP capacities (VP/KB capacity minus KB-derived capacity) were 144 mAh g^{-1} for LVP/KB(4:6), 95 mAh g^{-1} for LVP/KB(5:5), 15 mAh g^{-1} for LVP/KB(6:4), and 7.4 mAh g^{-1} for LVP/KB(7:3), respectively.

Table S2. Summary of electrochemical properties of representative Mg^{2+} battery cathodes based on oxide or polyanion compounds operating at room temperature.

Cathode	Average potential/ V vs. Mg^{2+}/Mg	Capacity / mAh g^{-1} (per composite)	Current / mA g^{-1} (C-rate)	Temp.	Cyclability (cycles)	Carbon contents (Carbon source)	Electrolyte	Ref.
Oxide								
$MgMn_2O_4$	1.9	270 (189)	-	R.T.	-	30% (AB)	$Mg[B(HFIP)_4]_2$/G3	2
$MgMn_2O_4$	1.9	100 (96)	5 (0.04C)	25 ° C	-	4% (CNT)	$Mg[B(HFIP)_4]_2$/G3	3
α-MnO_2	2.5	110 (99) 218 (192)	10	R.T.	-	10% (CB)	$Mg[TFSA]_2$/G3 $Mg[Al(HFIP)_4]_2$/G3	4
$ZnMnO_3$	1.9	93 (84)	3.98	30 ° C	52% (25)	10% (AB)	$Mg[B(HFIP)_4]_2$/G3	5
$V_2O_5.H_2O$ @rGO	2.4	115 (77)	1000 (3.3C)	20 ° C	81% (200)	3.4% (rGO) + 30% (AB)	$Mg(TFSA)_2$/AN	6
V_2O_5 (nanostructured)	0.8	160	20 (1/15C)	R.T.	100% (50)	-	$Mg(ClO_4)_2$/AN	7
V_2O_5 gel	2.2	600 (450)	1000 (3.3C)	R.T.	80% (35)	25% (AB)	$Mg(ClO_4)_2$/AN	8
V_2O_5 - P_2O_5 (amorphous)	2.7	121 (90)	5 (1/25C)	R.T.	-	25% (AB)	$Mg(ClO_4)_2$/AN	9
$NH_4V_sO_{10}$	2.3	175 (158)	42 (1/5C)	25 ° C	100% (100)	10% (CB)	$Mg(ClO_4)_2$/AN	10
Polyanion								
$K_2(VO)_2(HPO_4)_2(C_2O_4)\cdot4.5H_2O$	3.2	121(109)	109 (1C)	R.T.	87% (1500)	30% (KB)	$Mg(ClO_4)_2$/PC	11
$MnSiO_4$	1.6	244 (179)	8.3(1/60C)	25 ° C	-	20% (AB)	$Mg(TFSA)_2$/AN	12
UC-$FePO_4$	2.0	170 (85)	8.5(1/20C)	25 ° C	75% (30)	50% (KB)	$Mg(TFSA)_2$/AN	13
		80 (40)	85 (1/2C)		-		$Mg(TFSA)_2$/DMC	
		110 (55)	85 (1/2C)		-		$Mg(BF_4)_2$/DMC	
		170 (85)	85 (1/2C)		77% (100)		$Mg(TFSA)_2$ + $SBPBF_4$/DMC	
$FePO_4F$	2.5	35 (21)	14 (1/20C)	25 ° C	-	40% (AB)	$Mg(TFSA)_2$/AN	14
UC-$V_2(PO_4)_3$	3.3	200 (100)	131 (1C)	R.T.	76% (100)	50% (KB)	$Mg(TFSA)_2$ + $SBPBF_4$/DMC	**This work**

R.T.: Room temperature
AB: Acetylene black
CB: Carbon black
CNT: Carbon nanotube
rGO: Reduced graphene oxide
KB: Ketjen black
HFIP:1,1,1,3,3,3-hexafluoro-2-propanol
TFSA: (trifluoromethanesulfonyl)amide
AN: acetonitrile
DME: 1,2-dimethoxyethane
G3: triglyme
PC: propylene carbonate

Curves fitting results of *in-situ* X-ray Absorption Fine Structure (XAFS) measurements

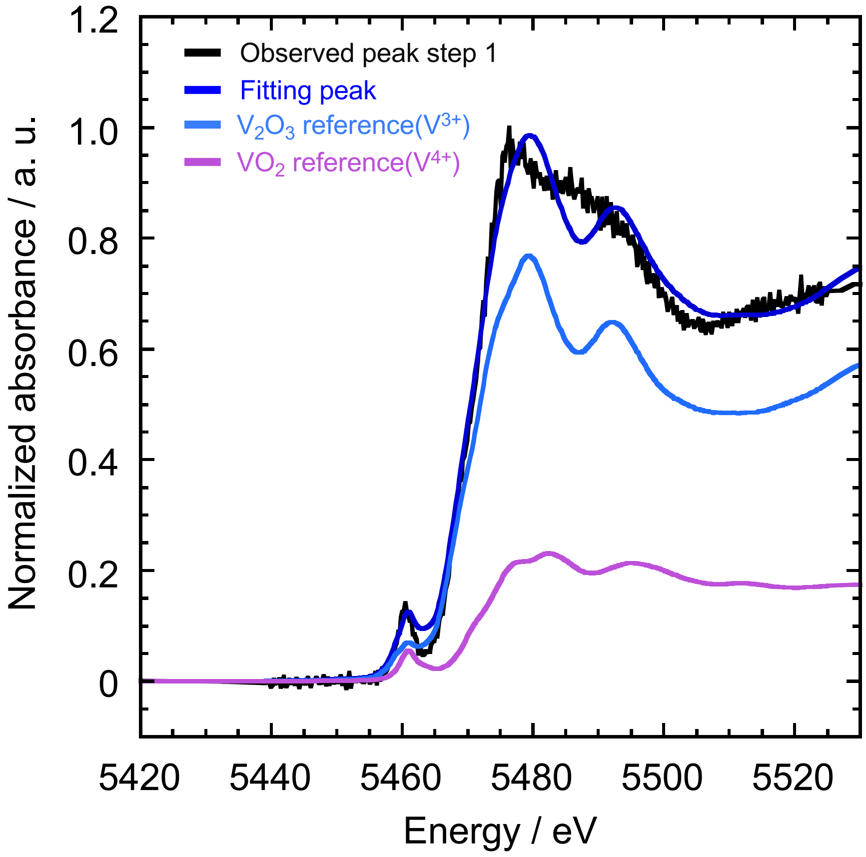

Figure S10. Typical curve-fitting results for *in-situ* XAFS measurements of VP/KB(5:5) corresponding to step 1 in Fig. 4 (main manuscript). The curve was fitted using V_2O_3 (V^{3+}) and VO_2 (V^{4+}) as references.

In-situ **XRD measurements of LVP/KB(5:5) using Li$^+$-based electrolyte**

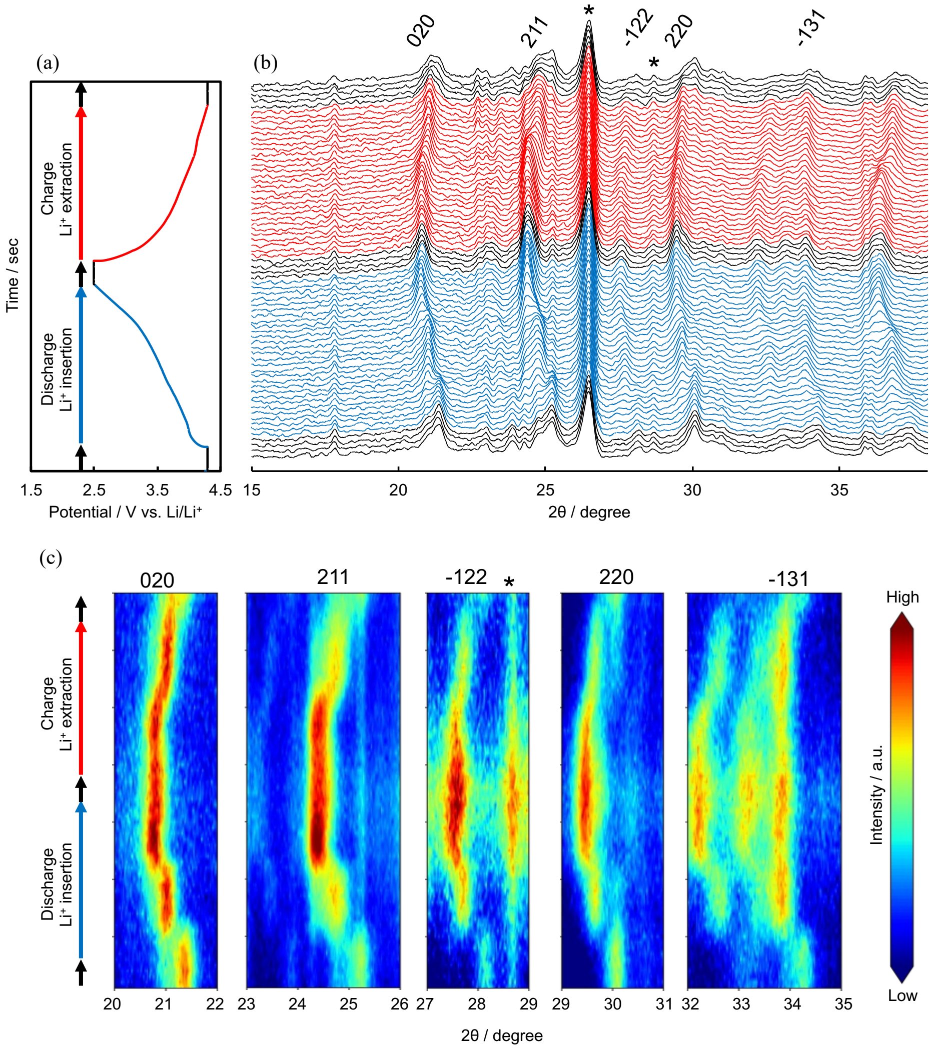

Figure S11. (a-c) *In-situ* XRD of LVP/KB(5:5): **(a)** Charge–discharge profile of LVP/KB(5:5) in the *in-situ* XRD cell (see Experimental) using a Li$^+$-based electrolyte (1 M LiPF$_6$/EC:DEC (1:1)) at 25 °C with Li metal as the counter electrode. The charge–discharge potential range was set at 2.5–4.3 V *vs.* Li/Li$^+$ (corresponding to 1.8–3.6 V *vs.* Mg/Mg^{2+}) and the charge-discharge rate was 0.2C-rate. **(b)** *In-situ* XRD patterns during charge-discharge of LVP/KB(5:5) in the 15−40° angular range. Asterisks denote reflections from cell components. **(c)** Contour plot of *in-situ* XRD patterns in the 20−22°, 23-26°, 27−29°, 29−31° and 32−35° angular ranges, in which peaks corresponding to the lattice planes of monoclinic Li$_3$V$_2$(PO$_4$)$_3$ (JCPDS No. 72-7074) can be observed. Prior to the *in-situ* XRD measurements, the cell was charged under constant-current to 4.3 V *vs.* Li/Li$^+$ at 0.2C-rate.

Galvanostatic intermittent titration technique (GITT) of VP/KB(5:5) using Mg^{2+} based electrolyte

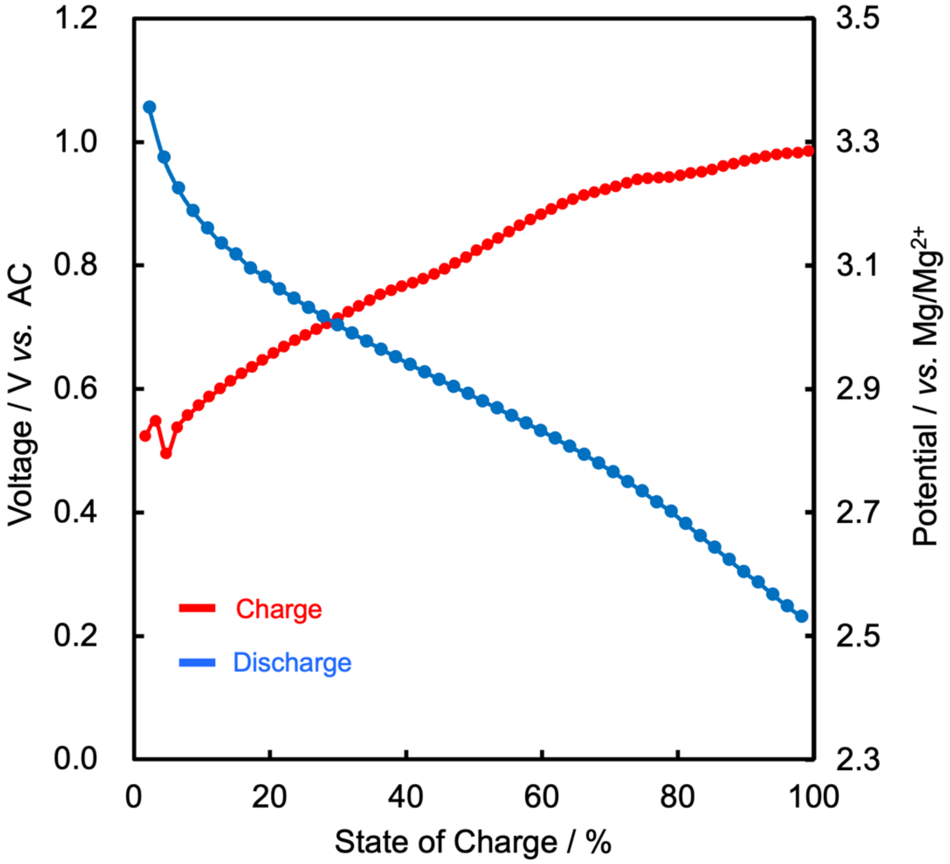

Figure S12. Plot of the potential at the end of the relaxation process using GITT for the charge and discharge processes. GITT was performed in the potential range of 0.1−1.2 V *vs.* AC (corresponding to 2.6–3.5 V *vs.* Mg/Mg^{2+}) where electrolyte decomposition hardly occurs, and the current impression process for 60 s at the 1C-rate (1C-rate = 131.5 mAh g^{-1} of $V_2(PO_4)_3$ active material) and the relaxation process was repeated for 0.5 h.

Cycle performance of VP/KB(5:5) for Mg electrolyte

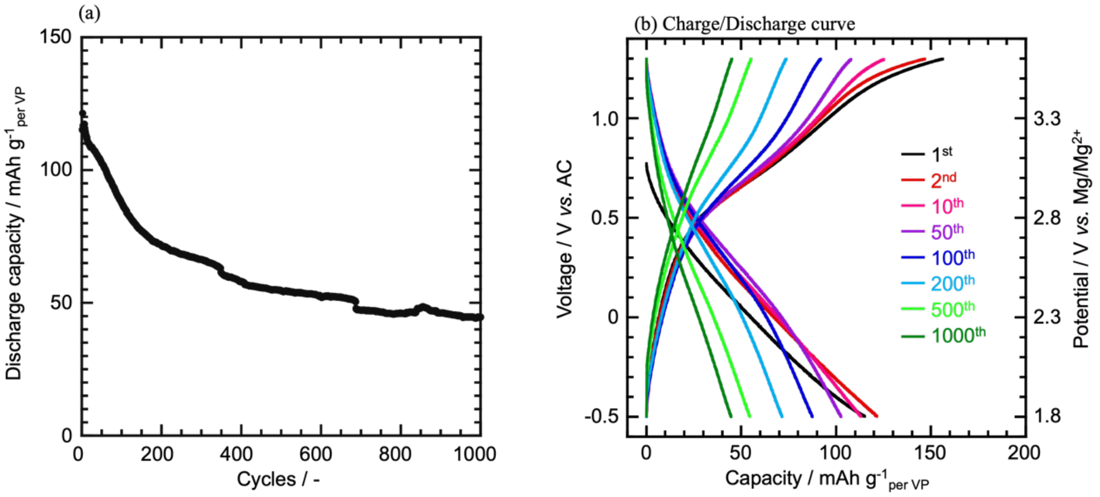

Figure S13. (a) Discharge capacity *vs.* cycle plot and (b) charge–discharge curves of VP/KB(5:5) during Mg^{2+} insertion/extraction. The charge–discharge potential range was set at -0.5–1.3 V *vs.* AC (corresponding to 1.8–3.6 V *vs.* Mg/Mg^{2+}) at 1C-rate (1C-rate = 131.5 mAh g^{-1} of the $V_2(PO_4)_3$ active material).

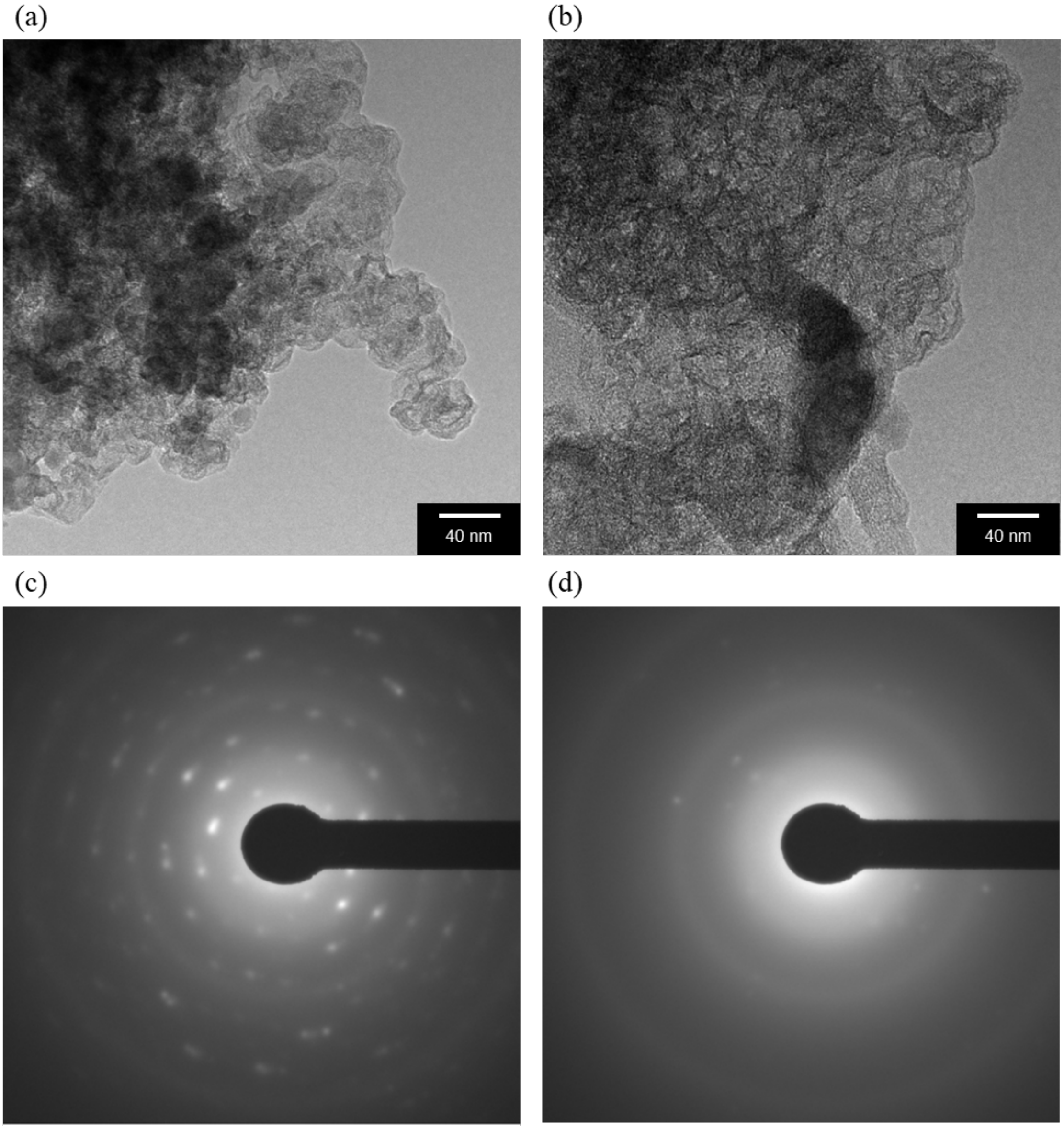

Figure S14. (a-d) TEM and electron diffraction images of VP/KB(5:5) before and after cycling. **(a, c)** pristine VP/KB(5:5), **(b, d)** VP/KB(5:5) over 1000 cycles. Pristine VP/KB(5:5) exhibits a diffraction pattern that indicates the presence of VP/KB(5:5) crystals. The absence of a diffraction pattern for VP/KB(5:5) over 1000 cycles suggests that the crystal of VP/KB(5:5) collapsed after long-term cycling.

Reference

1 S.-C. Yin, H. Grondey, P. Strobel, M. Anne and L. F. Nazar, *J. Am. Chem. Soc.*, 2003, **125**, 10402–10411.

2 H. Kobayashi, Y. Fukumi, H. Watanabe, R. Iimura, N. Nishimura, T. Mandai, Y. Tominaga, M. Nakayama, T. Ichitsubo, I. Honma and H. Imai, *ACS Nano*, 2023, **17**, 3135-3142.

3 K. Kajihara, D. Takahashi, H. Kobayashi, T. Mandai, H. Imai and K. Kanamura, *RSC Adv.*, 2021, **11**, 19076–19082.

4 X. Ye, H. Li, T. Hatakeyama, H. Kobayashi, T. Mandai, N. L. Okamoto and T. Ichitsubo, *ACS Appl. Mater. Interfaces*, 2022, **14**, 56685–56696.

5 T. Mandai, A. Kutsuma, M. Konya, Y. Nakabayashi and K. Kanamura, *Electrochemistry* , 2022, **90**, 027005–027005.

6 Q. An, Y. Li, H. Deog Yoo, S. Chen, Q. Ru, L. Mai and Y. Yao, *Nano Energy*, 2015, **18**, 265–272.

7 S. Tepavcevic, Y. Liu, D. Zhou, B. Lai, J. Maser, X. Zuo, H. Chan, P. Král, C. S. Johnson, V. Stamenkovic, N. M. Markovic and T. Rajh, *ACS Nano*, 2015, **9**, 8194–8205.

8 D. Imamura, M. Miyayama, M. Hibino and T. Kudo, *J. Electrochem. Soc.*, 2003, **150**, A753.

9 T. S. Arthur, K. Kato, J. Germain, J. Guo, P.-A. Glans, Y.-S. Liu, D. Holmes, X. Fan and F. Mizuno, *Chem. Commun.* , 2015, **51**, 15657–15660.

10 E. A. Esparcia Jr, M. S. Chae, J. D. Ocon and S.-T. Hong, *Chem. Mater.*, 2018, **30**, 3690–3696.

11 C. Li, L. Lin, W. Wu and X. Sun, *Small Methods*, 2022, **6**, e2200363.

12 Z. Feng, J. Yang, Y. NuLi, J. Wang, X. Wang and Z. Wang, *Electrochem. commun.*, 2008, **10**, 1291–1294.

13 Y. Orikasa, K. Kisu, E. Iwama, W. Naoi, Y. Yamaguchi, Y. Yamaguchi, N. Okita, K. Ohara, T. Munesada, M. Hattori, K. Yamamoto, P. Rozier, P. Simon and K. Naoi, *Chem. Mater.*, 2020, **32**, 1011–1021.

14 Z.-D. Huang, T. Masese, Y. Orikasa, T. Mori, T. Minato, C. Tassel, Y. Kobayashi, H. Kageyama and Y. Uchimoto, *J. Mater. Chem. A Mater. Energy Sustain.*, 2014, **2**, 11578–11582.